Non-Linear Regularized Attenuation Compensation for Microwave Breast Imaging

NASSER KAZEMI [1] AND ELISE FEAR [2] (Senior Member, IEEE)

[1]Département des sciences de la Terre et de l'atmosphére, Université du Québec à Montréal, Montreal, QC H3C3P8, Canada
[2]Department of Electrical and Software Engineering, University of Calgary, Calgary, AB T2N1N4, Canada

CORRESPONDING AUTHOR: NASSER KAZEMI (e-mail: kazemi_nojadeh.nasser@uqam.ca)

ABSTRACT We develop non-linear optimization algorithms for attenuation compensation of rapidly time-varying microwave signals in the context of breast imaging. The breast tissues attenuate the energy of the scattered wavefield as it travels within the medium. Compensating the attenuation effect is a challenging and typically unstable task. To address this issue, we develop inversion-based algorithms that take advantage of prior knowledge about the system. We formulate the attenuation compensation as a regularized non-linear cost function and introduce two efficient algorithms. The first algorithm assumes that the reflectivity series is smooth and follows a Gaussian distribution, i.e., ℓ_2 norm, and the second algorithm assumes that it can be cast as a sparse series, i.e., ℓ_1 norm. Also, both algorithms force the inverted quality factor to be close to an expected value based on previous evaluations of different models and datasets. Through testing of the algorithms on simulated and experimental datasets, we show that the proposed algorithms successfully compensate for attenuation. The images after attenuation compensation provide more accurate localization of the tumors and superior resolution when compared with conventional imaging practice.

INDEX TERMS Microwave imaging, optimization, sparsity, attenuation, breast tumor detection.

I. INTRODUCTION

Microwave imaging has been explored for the detection of breast cancer, as recently reviewed in [1], [2]. Approaches to medical microwave imaging include tomography and radar. With tomography, measurements of signals passing through the tissue are used to estimate the microwave frequency properties (permittivity and conductivity) by iteratively updating a model until simulations agree with measured data (e.g. [3], [4]). With radar, reflections from the tissues are collected at one or several locations, and focused to create an image indicating the locations of changes in properties (e.g. [5], [6], [7]). With both tomography and radar, a key challenge is detecting the tumor response in the background of the responses from the surrounding breast tissues. With radar, reflections from the skin and glandular tissues tend to dominate the responses from tumors [8]. Numerous signal processing and imaging approaches have been proposed to reduce these

reflections (e.g. [9], [10], [11], [12]), however, these techniques often result in a reduction of the tumor response as well. In addition, signals experience significant attenuation due to radial spreading and travel through lossy tissues. Compensation for this attenuation may permit improved detection of tumors.

Efforts have been made to address the attenuation effect in the imaging process [13], [14], [15]. These methods either compensate attenuation with pre-filtering the data or incorporate a frequency-dependent propagation effect inside the imaging algorithm. However, including attenuation in the imaging process may introduce instability in the imaging algorithm. An alternative approach decreases compensation of attenuation at greater depths, reducing noise [16]. In this article, we aim to provide a general and comprehensive attenuation model and efficient compensation algorithms to compensate for attenuation.

Posing attenuation compensation as an inverse problem results in the model that fits the data and also provides an opportunity to add *a priori* information about the desired outputs. Previous contributions model the data as a non-stationary time series (i.e., convolution of attenuated source signature with reflectivity series) [17] where the medium attenuates the signal with a constant quality factor (Q). In this model, attenuation is defined as a function of frequency and assumptions include source signature is minimum phase and the reflectivity series is white (i.e., Gaussian) [18]. The Gabor transform is applied, incorporating filters designed to compensate for attenuation. However, the source signature may not be a minimum phase and the reflectivity series is typically not white. In this article, we use the non-stationary model with constant Q, however, we do not impose constraints on the phase of the source signature and we assume that the reflectivity series is sparse (i.e., it has a limited number of non-zero coefficients). We also pose the problem as an inversion, instead of a filtering approach, and incorporate different regularization parameters to constrain our solution space. In Section II, we describe the data model and develop an alternating minimization algorithm to estimate the reflectivity series and Q, simultaneously. Possible choices of regularization terms in the inversion process are also discussed. The by-product of the algorithm is the attenuation-compensated data. In Section III, the proposed algorithms are tested on simulated and experimental datasets and images are formed, demonstrating the potential for this approach. Finally, Section IV summarizes key results.

II. METHODS

A. DATA MODEL

We assume that reflections of ultra-wideband pulses of microwave signals are available at a set of receiver locations. To form radar-based microwave images, a delay-and-sum (DAS) beamforming approach may be used. First, the clutter and reflections from the skin layer must be reduced. We use the neighborhood-based algorithm proposed in [19] to facilitate the reduction of skin reflections and this also results in a time-domain signal. The DAS algorithm may be written as:

$$\mathbf{I}(\mathbf{x}) = \sum_{\mathbf{x}'} \sum_{t} d^{sb}\left(t, \mathbf{x}'\right) \; G\left(\mathbf{x}; t, \mathbf{x}'\right) \qquad (1)$$

where d^{sb} is the data after reduction of clutter and the skin response, $\mathbf{x}'$ is the position of receiver antennas in space, $\mathbf{x}$ is the spatial position inside the imaging volume and G is Green's function. In the case of conventional DAS, the Green's function is

$$G(\mathbf{x}; t, \mathbf{x}') = \delta\left(t - \tau\left(\mathbf{x} - \mathbf{x}'\right)\right) \qquad (2)$$

where $\tau(\mathbf{x} - \mathbf{x}') = \frac{2|\mathbf{x} - \mathbf{x}'|}{v_p}$ is the time delay, and v_p is the phase velocity of the medium of interest.

To improve the performance of DAS imaging, we propose to compensate for attenuation before skin-interface suppression and then apply the DAS method to provide images

$$\mathbf{I}(\mathbf{x}) = \sum_{\mathbf{x}'} \sum_{t} d_Q^{sb}\left(t, \mathbf{x}'\right) \; G\left(\mathbf{x}; t, \mathbf{x}'\right) \qquad (3)$$

where d_Q^{sb} is attenuation compensated and skin-interface suppressed data.

The recorded microwave data at each receiver antenna can be modeled as a non-stationary time series. Attenuation of waves propagating through the breast tissues causes non-stationary behavior in the data [8]. We model the input-output relationship for this system, in the frequency domain, as

$$d_n(f) = w(f) \int_{-\infty}^{\infty} \beta(t, f)\left[r(t) + r_n(t)\right]$$
$$\times \exp(-j2\pi f t)\, dt + n(f), \qquad (4)$$

where $d_n(f)$ is the noisy recorded signal, $w(f)$ is the excitation pulse, $r(t)$ is the impulse response of the breast interior, $r_n(t)$ is the impulse response of clutter and the layer of skin surrounding the breast, β represents the time-frequency response of the attenuation, $n(f)$ is measurement noise, f is temporal frequency, t is time, and $j = \sqrt{-1}$ is the imaginary unit. Equation (4) is a non-stationary convolution of reflectivity series with frequency-dependent attenuation term β and the pulse w [20]. The simplest form of the attenuation response is

$$|\beta(t, f)| = \exp(-\alpha t), \qquad (5)$$

where $\alpha = \frac{\pi |f|}{Q}$ is frequency-dependent constant quality factor, Q is quality factor, and $|\cdot|$ denotes absolute value. Here, attenuation is defined as the inverse of the quality factor. Also, the α term defines the overall damping factor of energy in the time domain, which is greater for higher frequencies. The β term is complex, hence, we also need to define its phase. The notation here follows conventions from geophysics, so α and β are defined differently than is typical for electromagnetics. It is worth noting that in our approach we assume that the pulse is known. However, the algorithm is not restricted to only minimum phase pulses.

In matrix-vector notation, (4) reads

$$\mathbf{d} = \mathbf{W}\mathbf{A}\,\mathbf{r}, \qquad (6)$$

where $\mathbf{r} = (r[0], r[1], \ldots, r[M-1])^T$ is reflectivity series, $\mathbf{W}$ is a convolution matrix of transmitted pulse $\mathbf{w} = (w[0], w[1], \ldots, w[L-1])^T$, $\mathbf{A}$ is attenuation matrix, and $\mathbf{d} = (d[0], d[1], \ldots, d[N-1])^T$ is the recorded microwave data. We stress that $N = M + L - 1$. It is also worth mentioning that $\mathbf{W}$ with dimensions $N \times M$ has a Toeplitz structure

and can be written as

$$
\mathbf{W} = \begin{pmatrix} w[0] & & & \\ w[1] & w[0] & & \\ w[2] & w[1] & w[0] & \\ \vdots & & \ddots & \\ & & w[L-1] & w[L-2] \\ & & & w[L-1] \end{pmatrix}
\tag{7}
$$

Using this framework, three different approaches to attenuation compensation are developed, as detailed in the next sections.

B. LEAST-SQUARES ATTENUATION COMPENSATION (LSQ)

To compensate for attenuation, we propose to solve the general cost function of

$$
\{\hat{\mathbf{r}}, \hat{\mathbf{A}}\} = \underset{\mathbf{r}, \mathbf{A}}{\arg\min} \quad \|\mathbf{WAr} - \mathbf{d}\|_2^2 + \mathcal{R}_r(\mathbf{r}) + \mathcal{R}_A(\mathbf{A}).
\tag{8}
$$

where $\mathcal{R}_r(\mathbf{r})$ and $\mathcal{R}_A(\mathbf{A})$ are regularization terms for reflectivity and quality matrix, respectively. In this section, for the sake of simplicity, we ignore the regularization terms and pose the problem as

$$
\{\hat{\mathbf{r}}, \hat{\mathbf{A}}\} = \underset{\mathbf{r}, \mathbf{A}}{\arg\min} \quad \|\mathbf{WAr} - \mathbf{d}\|_2^2.
\tag{9}
$$

We solve the cost function of (9) with an alternating minimization method. First, we fix the $\mathbf{A}$ matrix, by using a realistic Q as an initial estimation, and solve

$$
\hat{\mathbf{r}}^k = \underset{\mathbf{r}}{\arg\min} \quad \|\mathbf{WA}^k\mathbf{r} - \mathbf{d}\|_2^2,
\tag{10}
$$

where k is iteration number. Equation (10) has a closed form solution

$$
\hat{\mathbf{r}}^k = \left(\mathbf{W}_Q^T\mathbf{W}_Q\right)^{-1} \mathbf{W}_Q^T\mathbf{d}.
\tag{11}
$$

where $\mathbf{W}_Q = \mathbf{WA}^k$. Note that we assume that the transmitted pulse is known. Next, we use the updated reflectivity series and update the $\mathbf{A}$ matrix by solving

$$
\hat{\mathbf{A}}^{k+1} = \underset{\mathbf{A}}{\arg\min} \quad \|\mathbf{WAr}^k - \mathbf{d}\|_2^2.
\tag{12}
$$

Equation (12) is a non-linear least-squares minimization problem. It is worth mentioning that the $\mathbf{A}$ matrix is a non-Toeplitz matrix. To efficiently solve (12), we change the cost function to a non-linear parameter estimation problem for Q

$$
\hat{Q}^{k+1} = \underset{Q}{\arg\min} \quad \|\mathcal{F}\left(Q, \mathbf{w}, \mathbf{r}^k\right) - \mathbf{d}\|_2^2.
\tag{13}
$$

Non-linear parameter estimation techniques [21] can be used to solve (13). Because the evaluation of (13) for each Q candidate is fast, i.e., simple matrix-vector multiplication, and the possible model domain for Q is reasonably bounded, we can simply implement a parabolic search method with three values of Q in each iteration. The initial Q values are chosen to be $Q_1 < Q_2 < Q_3$. In each iteration, we evaluate (13) using

---

Algorithm 1: Alternating Minimization Algorithm for Attenuation Compensation.

Require: W, d
   Initialize: $\mathbf{A}^0$, $k = 0$
   While not converged
1: *Solve for* $\mathbf{r}^k$ *by using* (11)
2: *Solve for* Q^{k+1} *by minimizing* (13)
3: *Update* $\mathbf{A}^{k+1}$ *byusing* Q^{k+1}
4: *Update* $k \leftarrow k + 1$
   If converged
   Output
   $\mathbf{r} \leftarrow \mathbf{r}^k$
   $Q \leftarrow Q^k$

---

these three Q values and define the new minimum and its corresponding Q value (Q_{new}) with parabolic interpolation. In the next iteration, if $Q_{new} < Q_2$ then the new three candidates are $Q_1 < Q_{new} < Q_2$. On the other hand, if the $Q_{new} > Q_2$ then the new three candidates are $Q_2 < Q_{new} < Q_3$. We repeat the process until convergence. Finally, matrix $\hat{\mathbf{A}}^{k+1}$ is built from estimated $\hat{Q}^{k+1}$.

Equations (11) and (13) are solved alternatively until the algorithm converges to the desired solution. The pseudo-code of the algorithm is represented in Algorithm 1. In Algorithm 1, $\mathbf{A}^0$ is built from our initial estimation of Q which can be the quality factor of fatty breast tissue. The output of the algorithm is the estimated reflectivity series $\mathbf{r}$ and the average quality factor Q for each channel. Convolving the estimated reflectivity series with the excitation pulse results in estimating the attenuation-compensated data.

C. DAMPED LEAST-SQUARES ATTENUATION COMPENSATION (DLSQ)

Posing attenuation compensation as an inverse problem provides an opportunity to include *a priori* information about the reflectivity and quality factor. For example, if the quality factor of fatty breast tissues is approximately known, then we can add a regularization term that minimizes the difference between the estimated quality factor and the quality factor of the tissues. Also, one possible regularization term for the reflectivity series is to assume that the reflectivity series has a minimum norm in ℓ_2 sense. Considering these constraints changes the general cost function of (8) to

$$
\{\hat{\mathbf{r}}, \hat{\mathbf{A}}\} = \underset{\mathbf{r}, \mathbf{A}}{\arg\min} \quad \|\mathbf{WAr} - \mathbf{d}\|_2^2 + \lambda_r\|\mathbf{r}\|_2^2 + \lambda_Q\|Q - Q_0\|_2^2,
\tag{14}
$$

where λ_r and λ_Q are regularization parameters, and Q_0 is the approximate quality factor for the fatty tissues in the breast. There are several interesting algorithms that can provide a good approximation for Q_0 [17], [20], [22], [23], [24]. Equation (14) can also be solved with Algorithm 1. However, in this case, (10) changes to

$$
\hat{\mathbf{r}}^k = \underset{\mathbf{r}}{\arg\min} \quad \|\mathbf{WA}^k\mathbf{r} - \mathbf{d}\|_2^2 + \lambda_r\|\mathbf{r}\|_2^2.
\tag{15}
$$

Algorithm 2: FISTA Algorithm for Solving (19).

Require: d, **B**, λ_r, η

Initialize: $\mathbf{r}^0 = \mathbf{0}$, $\mathbf{r}^0_{thresh} = \mathbf{r}^0$, $t_0 = 1$, $k = 1$, $T = \frac{\lambda_r}{2\eta}$

While not converged

$\mathbf{y} = \mathbf{r}^{k-1}_{thresh} - \frac{1}{\eta}\mathbf{B}^T\left(\mathbf{B}\mathbf{r}^{k-1} - \mathbf{r}\right)$

$\mathbf{r}^k = (|\mathbf{y}| - T)_+ \odot sign(\mathbf{y})$

$t_k = \frac{1}{2}\left(1 + \sqrt{1 + 4\,t^2_{k-1}}\right)$

$\mathbf{r}^k_{thresh} = \mathbf{r}^k + \frac{(t_{k-1}-1)(\mathbf{r}^k - \mathbf{r}^{k-1})}{t_k}$

$k \leftarrow k + 1$

If converged

Output

$\mathbf{r} \leftarrow \mathbf{r}^k$

Equation (15) has a closed form solution

$$\hat{\mathbf{r}}^k = \left(\mathbf{W}_Q^T\mathbf{W}_Q + \lambda_r\mathbf{I}\right)^{-1}\mathbf{W}_Q^T\mathbf{d}, \tag{16}$$

where $\mathbf{I}$ is an identity matrix with appropriate dimensions. One advantage of (15) compared to (10) is that it guarantees that the inverse of the $\mathbf{W}_Q^T\mathbf{W}_Q + \lambda_r\mathbf{I}$ matrix exists. Moreover, (13) changes to

$$\hat{Q}^{k+1} = \underset{Q}{\operatorname{argmin}} \quad \|\mathcal{F}\left(Q, \mathbf{w}, \mathbf{r}^k\right) - \mathbf{d}\|_2^2 + \lambda_Q\|Q - Q_0\|_2^2. \tag{17}$$

Equation (17) can also be solved with the parabolic line search method similar to (13). Hence, for the cost function of (14), in Algorithm 1 instead of solving (11) and (13) we need to solve (16) and (17), respectively.

D. SPARSITY REGULARIZED LEAST-SQUARES ATTENUATION COMPENSATION (SLSQ)

The reflectivity series can also be cast as a sparse time series. This assumption is extensively implemented in different fields of studies [25], [26], [27], [28], [29], [30], [31], [32], [33], [34]. We use ℓ_1 norm to promote sparsity in the reflectivity series. Replacing this regularization term with the ℓ_2 norm assumption for the reflectivity series changes (14) to

$$\{\hat{\mathbf{r}}, \hat{\mathbf{A}}\} = \underset{\mathbf{r},\mathbf{A}}{\operatorname{argmin}} \quad \|\mathbf{W}\mathbf{A}\mathbf{r} - \mathbf{d}\|_2^2 + \lambda_r\|\mathbf{r}\|_1 + \lambda_Q\|Q - Q_0\|_2^2. \tag{18}$$

Equation (18) can also be solved with Algorithm 1. However, in this case, (10) changes to

$$\hat{\mathbf{r}}^k = \underset{\mathbf{r}}{\operatorname{argmin}} \quad \|\mathbf{B}\mathbf{r} - \mathbf{d}\|_2^2 + \lambda_r\|\mathbf{r}\|_1. \tag{19}$$

where $\mathbf{B} = \mathbf{W}\mathbf{A}^k$. Equation (19) is an $\ell_2 - \ell_1$ minimization problem and any $\ell_2 - \ell_1$ norm solver can be used to solve this cost function. In the interim, we use the fast iterative shrinkage-thresholding algorithm (FISTA) [35]. Details of the FISTA algorithm are represented in Algorithm 2.

In Algorithm 2, η is equivalent to the maximum eigenvalue of the $\mathbf{B}^T\mathbf{B}$ matrix, and $\odot$ stands for the Hadamard product. We use a power iteration algorithm [36], [37] to calculate η. Also, for the cost function of (18), the update equation for the

Q is the same as (17). Hence, in Algorithm 1, instead of solving Equations (11) and (13), we need to solve Equations (19) and (17), respectively.

Note that in all three variations on the attenuation compensation algorithms, we recover the attenuation compensated data by convolving the excitation pulse with the estimated reflectivity series. The algorithm designed to reduce the reflection from the skin layer [19] is then applied to these attenuation-compensated signals prior to the application of the DAS algorithm. Note that the images are calculated with 2 mm pixels.

E. PARAMETER SELECTION CRITERIA

There are different strategies for tuning the input parameters for LSQ, DLSQ, and SLSQ methods, namely λ_r, λ_Q, and Q_0. In this article, for simplicity, we use a trial and error approach to tune the regularization parameters λ_r and λ_Q. We assume values for Q_0 based on experience with the datasets.

In the DLSQ method, increasing the value of λ_r provides smoother reflectivity (i.e., minimum norm solution). By increasing the value of λ_Q, the estimated Q will be closer to Q_0. In the SLSQ method, increasing the value of λ_r provides sparser reflectivity (i.e., a smaller number of non-zero coefficients). By increasing the value of λ_Q, the estimated Q will be closer to Q_0. To automate the algorithm and fine-tune the regularization parameters, we can use Generalized Cross Validation (GCV) method [38], [39], [40]. The GCV method has been used in the past to tune inputs in cost functions with several regularization parameters. The method works on $\ell_2 - \ell_2$ and $\ell_2 - \ell_1$ cost functions [40]. The GCV method has been successfully used in tuning the regularization parameters for the deconvolution problem [41], [42]. Several interesting algorithms can provide a good approximation for Q_0 [17], [20], [22], [23], [24]. Since the evaluation of the cost function for different values of Q is not costly, we can use non-linear algorithms such as fast simulated annealing to define the Q without providing the Q_0 [43]. In other words, we use Q_0 to search for the Q in the neighborhood of Q_0, and we use λ_Q to define how close the solution is to Q_0.

F. DATASETS AND METRICS

Initially, the proposed algorithms are tested with a synthetic example. Next, simulated and experimental datasets of increasing complexity are examined. All datasets have been previously reported, so are summarized briefly here.

Dataset D1 is a simple breast model that consists of a 10-cm hemispherical skin layer filled with canola oil and containing a tumor (similar to [44]). Simulations of the breast model are performed with the finite difference time domain method (SEMCAD, SPEAG, Switzerland); the model is illuminated with an ultrawideband pulse using a custom antenna (BAVA-D) and reflections are collected as the antenna is scanned to 140 locations around the model. Dataset D2 is the corresponding experimental data, however, 3 scans of the model are collected to assess consistency [45]. Here, reflections of

ultra-wideband signals are collected using a prototype imaging system [46]. Datasets D1 and D2 test the algorithms in a simple scenario and allow for the comparison of simulated and experimental data.

Dataset D3 contains simulated reflections collected from a realistic breast model created from a magnetic resonance scan of a patient [47]. Here, the ultrawideband antenna is scanned to 300 locations around the model. This model has realistic tissue distributions and shape, providing a more complex testbed for the proposed algorithms.

Dataset D4 is a scan of a breast cancer patient who had a tumor located in her right breast. As reported in [48], patient scans were part of a study approved by the University of Calgary Conjoint Health Research Ethics Board (study E-24098); patients provided written informed consent. Reflections of the breast are collected at 140 locations by scanning a single antenna around the tissue, again using the prototype described in [46].

For datasets D1-D3, the response of only the tumor is extracted at single receivers by subtracting the data acquired with and without the tumor present in the model. This isolation of the tumor response is repeated for signals after attenuation compensation. In the case of patient data (D4), we do not have access to the tumor-free case; however, we analyze the skin-suppressed data before and after compensation.

To quantitatively compare the performances of algorithms on images, we use two metrics. The first metric compares the estimated tumor locations in the images to the known location. The second metric evaluates the focusing of tumors in the normalized 3D images. For a fair comparison, we first normalize the intensity values of the images, and values higher than 0.75 are categorized as tumor response. Then, we define the number of pixels in the images as $Total$ and the number of pixels in tumor regions as $Tumor$ and the *localization ratio* as $Lr = 100 \times \frac{Tumor}{Total}$. The smaller the number, the more localized the tumor region.

III. RESULTS

A. SYNTHETIC EXAMPLE

We generate a synthetic time series that mimics the recorded microwave data received by the antenna by convolving a transmitter's signature with a sparse reflectivity series. Two time series with and without attenuation are considered. Fig. 1(a) and (b) show the transmitter's signature, which is a 40-degree phase rotated Ricker wavelet and the sparse reflectivity series, respectively. Fig. 1(c) is the stationary data without attenuation, i.e., $\mathbf{d} = \mathbf{Wr}$, and Fig. 1(d) is the non-stationary time series with attenuation, i.e., $\mathbf{d} = \mathbf{WAr}$. We use $Q = 25$. We simply convolve the transmitter's signature with the estimated reflectivity to recover the attenuation compensated dataset.

Fig. 2 shows the estimated reflectivity and attenuation compensated data by using LSQ, DLSQ, and SLSQ methods. In DLSQ method we use $Q_0 = 20$, $\lambda_r = 0.01$, and $\lambda_Q = 0.001$, and in SLSQ method we use $Q_0 = 20$, $\lambda_r = 0.001$, and $\lambda_Q = 0.004$. The results show that the SLSQ approach outperforms
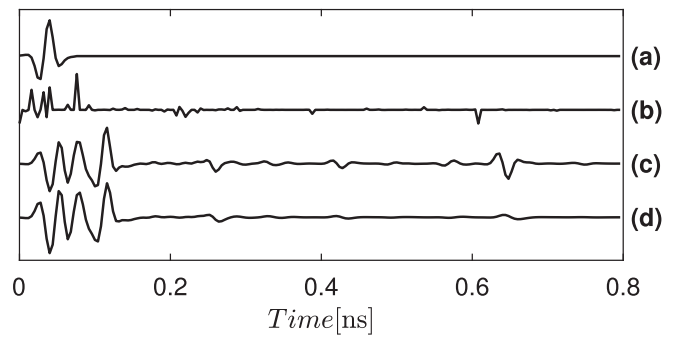
FIGURE 1. Synthetic data for testing attenuation compensation. Each line is offset for clarity and labelled as (a) Transmitter's signature. (b) Sparse reflectivity series. (c) Data without attenuation. (d) Data with attenuation.
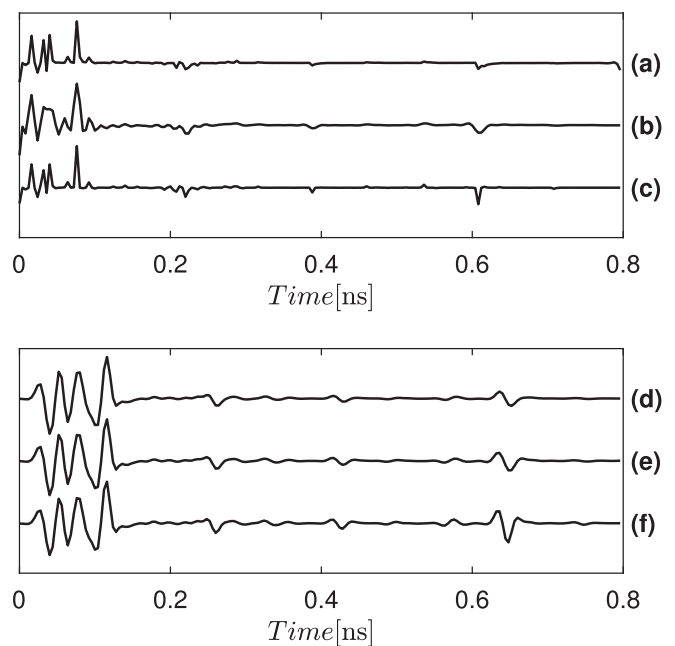
FIGURE 2. Performances of attenuation compensation algorithms on the synthetic data shown in Fig. 1(d). In the upper plot, lines a), b), and c) are offset for clarity and correspond to the estimated reflectivity series obtained with LSQ, DLSQ and SLSQ. In the lower plot, lines d), e), and f) are offset for clarity and correspond to the estimated data after attenuation compensation by using LSQ, DLSQ, and SLSQ methods, respectively.

LSQ and DLSQ methods in estimating the reflectivity series and quality factor. The estimated quality factors for LSQ, DLSQ, and SLSQ are 40, 31, and 24, respectively. Moreover, in the LSQ method, the $\mathbf{W}_Q^T \mathbf{W}_Q$ matrix is close to singular, and the inverse of a such matrix can be erroneous and can introduce instability in the inversion. As mentioned in the parameter selection section, the GCV function can optimally define the regularization parameters. For example, in the method of SLSQ, the tuneable regularization parameters are λ_r and λ_Q. To automatically define the optimal parameters, we use the GCV function that is designed for the $\ell_2 - \ell_1$ cost functions [40]. The GCV function for the SLSQ cost function
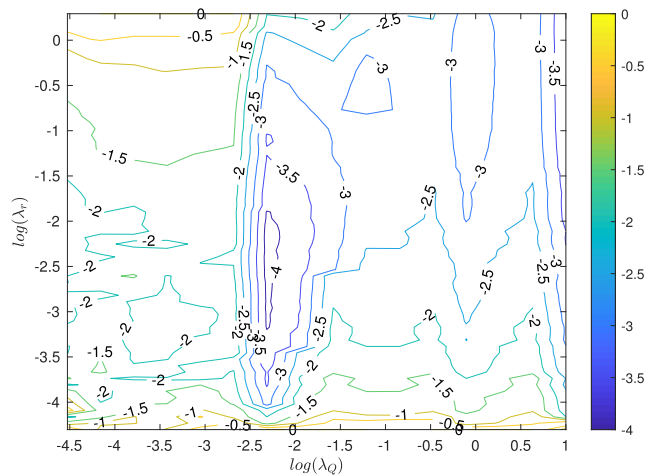
FIGURE 3. Logarithm of normalized GCV function with the stability coefficient C = 2 for fine tuning the regularization parameters within SLSQ method for the synthetic data represented in Fig. 1.

in (18) is as follows

$$GCV(\lambda_r, \lambda_Q) = \frac{\|\mathbf{WA}(\lambda_r)\mathbf{r}(\lambda_r) - \mathbf{d}\|_2^2 + \lambda_Q \|Q - Q_0\|_2^2}{(N - C\|\mathbf{r}\|_0)^2},$$

(20)

where $C \geq 1$ is the stability coefficient, $\|\mathbf{r}\|_0$ is the ℓ_0-norm that counts the number of nonzero elements in the reflectivity series $\mathbf{r}$, and N is the length of $\mathbf{r}$. The optimal regularization parameters correspond with the minimum of the GCV function in (20). To define the parameters, we define possible ranges for λ_r and λ_Q. Then, for each combination of λ_r and λ_Q, we run the SLSQ algorithm and evaluate the GCV function. Fig. 3 shows the normalized GCV function on a logarithmic scale. When the $\log(GCV)$ is less than -2.5, the algorithm provides satisfactory results. It is clear that the fine-tuned regularization parameters with trial and error nicely reside within the acceptable ranges for the parameters. The minimum of the GCV function provides optimal values for the regularization parameters automatically. However, we must run the algorithms several times to evaluate the GCV function. To reduce the computational cost of the algorithms, we tune the parameters with a trial-and-error approach.

B. DATASET D1

Dataset D1 contains a circular tumor with 16 mm diameter centered at X= 25 mm, Y= 0 mm, Z= −17.3 mm. Fig. 4(a) shows the time series corresponding to channel 22 in the dataset, as well as the response of only the tumor (this channel has a strong tumor response). After attenuation compensation, the response of channel 22 along with the tumor-only response are represented in Fig. 4(b)–(d), respectively. Table 1 summarizes the parameters used for the attenuation compensation algorithms. The compensated data using all three methods show an amplitude boost in the later arrivals and phase changes in the data.
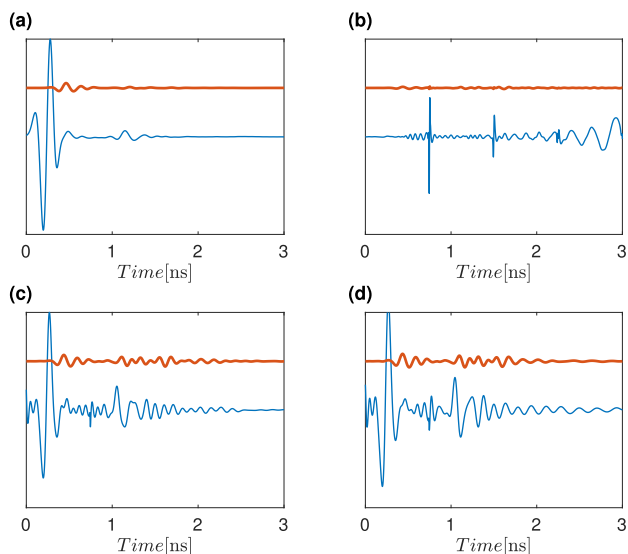
FIGURE 4. Performances of attenuation compensation algorithms on the simulated data D1. (a) measured dataset at channel 22. The offset red trace is the tumor only response of the original data. (b), (c), and (d) are the estimated data and tumor only response after attenuation compensation by using LSQ, DLSQ, and SLSQ methods on a), respectively.

TABLE 1. Input Parameters for Compensation Algorithms Using Simulated Datasets D1 and D3

Compensation algorithm	λ_r	λ_Q	Q_0	Q_1	Q_2	Q_3
LSQ	0.0	0.0	7	1	5	10
DLSQ	0.001	0.001	7	1	5	10
SLSQ	0.0005	0.001	7	1	5	10

To provide accurate images, data should have reliable low, mid, and high-frequency contributions. After attenuation compensation, the energy lost due to attenuation is recovered; the tumor response differs in amplitude and phase from the tumor response before attenuation compensation. The result of the LSQ method shows a ringing effect, and in most channels gives unstable solutions as the algorithm tries to invert a singular matrix. On the other hand, DLSQ and SLSQ methods successfully recover the signal.

Next, we use the data with and without attenuation compensation to provide DAS images.

Fig. 5 shows the 2D image at the location corresponding to the maximum response in the axial plane that is extracted from the 3D imaging volume. The images show that the conventional approach provides two tumor responses where the ideal response is a single tumor. As expected, the LSQ-DAS image shows an unstable result. However, the DLSQ-DAS and SLSQ-DAS images show promising results and match well with the ideal response in the model.

To compare the performances of the algorithm, we calculate the maximum amplitude location of the tumor in the images and compare it with the ideal location. Table 3 shows the estimated tumor location by using DAS, LSQ-DAS, DLSQ-DAS, and SLSQ-DAS methods. Table 4 shows the localization ratio values of the 3D images. After attenuation compensation,
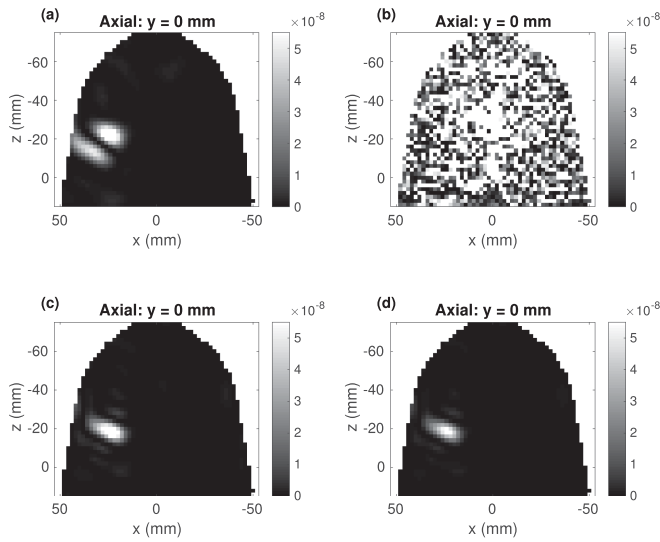
FIGURE 5. Axial images of simple synthetic dataset (D1). (a) DAS image. (b) LSQ-DAS image. (c) DLSQ-DAS image. (d) SLSQ-DAS image.

TABLE 2. Input Parameters for Compensation Algorithms Using the Experimental Datasets D2 and D4

Compensation algorithm	λ_r	λ_Q	Q_0	Q_1	Q_2	Q_3
LSQ	0.0	0.0	17	10	15	20
DLSQ	0.5	0.001	17	10	15	20
SLSQ	0.5	0.001	17	10	15	20

TABLE 3. Ground Truth and Estimated Locations of Tumor in Simulated and Experimental Datasets

Dataset	GROUND TRUTH	DAS	LSQ-DAS	DLSQ-DAS	SLSQ-DAS
D1	$25, 0, -17.3$	$24, 0, -22$	$0, 0, -8$	$24, 0, -18$	$24, 0, -18$
D2-type1	$20, 0, -49$	$16, -4, -48$	$0, 8, -78$	$14, -4, -48$	$16, -4, -48$
D2-type2	$20, 0, -49$	$16, -4, -48$	$16, -2, -50$	$16, -2, -50$	$16, -2, -50$
D2-type3	$20, 0, -49$	$18, -4, -50$	$0, 8, -80$	$16, -2, -50$	$16, -2, -50$
D3	$-19, 0, -27$	$-22, -2, -32$	$-16, 0, -26$	$-16, 0, -26$	$-18, 0, -26$
D4- Right breast	Unkown	$34, -12, -14$	$-14, 4, -16$	$-22, 0, -16$	$-24, -2, -20$

Locations are in cartesian coordinates x, y, z, respectively, and units are in (mm).

TABLE 4. Localization Ratios (L_r) in Normalized 3D Images of the Simulated and Experimental Datasets

Dataset	DAS	DLSQ-DAS	SLSQ-DAS
D1	4.5%	3.7%	3.6%
D2-type1	4.3%	2.8%	2.8%
D2-type2	4.3%	3.0%	3.0%
D2-type3	4.4%	2.8%	2.8%
D3	8.3%	6.8%	6.9%
D4- Right breast	4.1%	2.5%	2.5%

images show at least 1% higher localization compared to that of the DAS image. Since, the LSQ method does not provide stable solutions, for other datasets, we do not show and discuss the results of LSQ and LSQ-DAS methods.

C. D2 DATASET

Dataset D2 contains a circular tumor with 16 mm diameter centered at X= 20 mm, Y= 0 mm, Z= −49 mm. The data
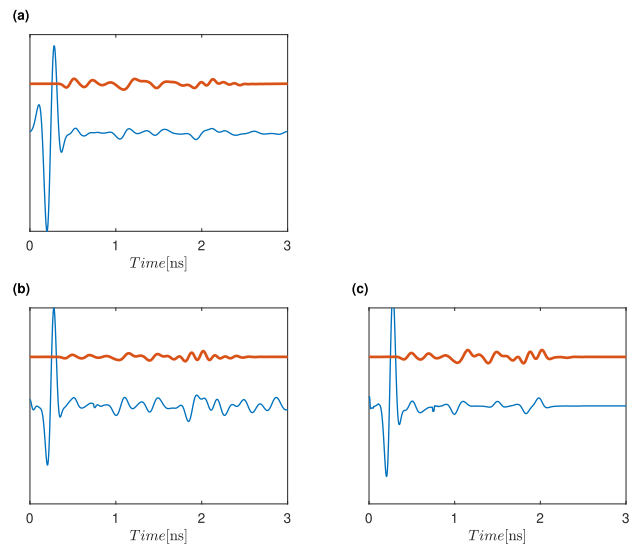
FIGURE 6. Performance of attenuation compensation algorithms on the original and skin-suppressed experimental data D2-type3 channel 52. (a) measured dataset at channel 52 (blue color) after skin removal (red color). (b) and (c) are the estimated data after attenuation compensation of (a) by using DLSQ and SLSQ methods, respectively.
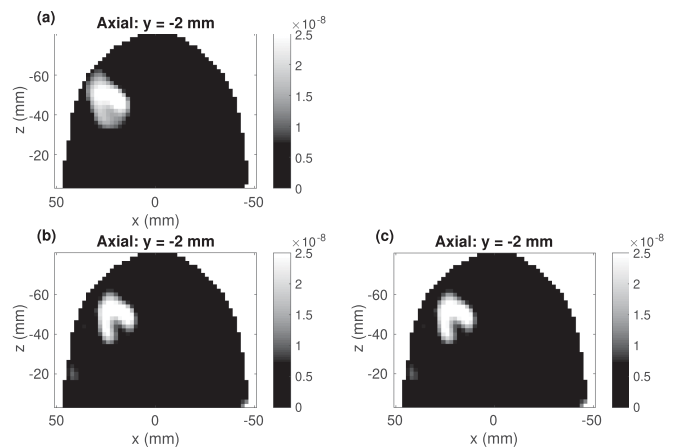
FIGURE 7. Axial images of measured dataset D2-type3. (a) DAS image. (b) DLSQ-DAS image. (c) SLSQ-DAS image.

is acquired three times to analyze the repeatability of the experiment (D2-type1, D2-type2, and D2-type3).

Fig. 6(a) shows a channel of one dataset before and after skin attenuation. The dataset shows less attenuation compared with the D1 dataset. The inversion parameters are summarized in Table 2.

Fig. 6(b) and (c) show the data after attenuation compensations by using the DLSQ and SLSQ methods. Data after attenuation compensation show more balanced energy between early and late arrival times.

Next, DAS images are created. Fig. 7 shows the axial sections of the images computed by the DAS, DLSQ-DAS, and SLSQ-DAS methods. The images computed by DLSQ-DAS and SLSQ-DAS methods show better localization compared to the DAS image.
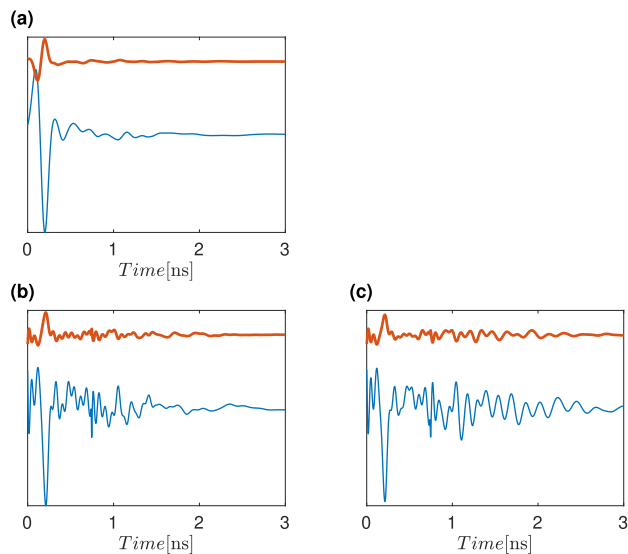
FIGURE 8. Performance of attenuation compensation algorithms on the simulated data D3. (a) original data after low-pass filtering at channel 280. The red color trace is the tumor only response of the original data. (b) and (c) are the estimated data and tumor only response after attenuation compensation by using DLSQ and SLSQ methods on (a), respectively.

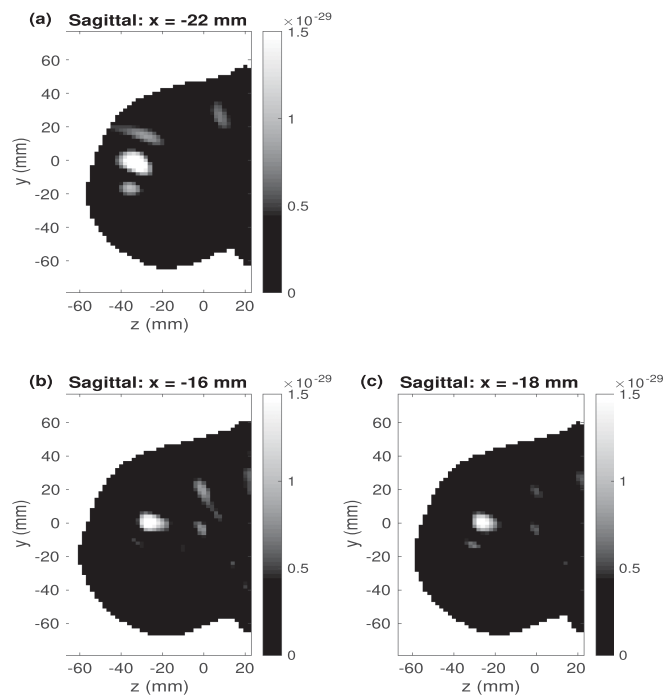**FIGURE 9.** Coronal images of realistic simulated dataset D3. (a) DAS image. (b) DLSQ-DAS image. (c) SLSQ-DAS image.

FIGURE 10. Sagittal images of realistic simulated dataset D3. (a) DAS image. (b) DLSQ-DAS image. (c) SLSQ-DAS image.

The algorithms are applied to all 3 datasets and results demonstrate consistency for the DLSQ-DAS and SLSQ-DAS algorithms. Table 3 summarizes the location of tumors calculated with different attenuation algorithms, and Table 4 shows the localization ratios. Both DLSQ-DAS and SLSQ-DAS methods successfully locate the tumor in the images. The localization ratios, after attenuation compensation, show $\approx$ 1.5% more focusing of tumor response on all three datasets.

D. D3 DATASET
The D3 dataset contains a region of glandular tissue, along with a single circular tumor of 15 mm diameter centered at X=−19 mm, Y=0 mm, Z=−27 mm. The data show similar attenuation behavior to that of the D1 dataset.

Fig. 8(a) depicts the data at channel 280, where the data contains a significant tumor response. The data has no significant scattered energy after 1.5 ns, similar to the D1 dataset. Hence, we constrain the search space for the quality factor to be in the same range as the D1 dataset. The parameters are summarized in Table 1. Fig. 8 shows that the DLSQ and SLSQ methods successfully compensate for attenuation in this data.

Next, we use the data with the skin response removed, both with and without attenuation compensation, to create DAS images.

Figs. 9 and 10 show the coronal and sagittal sections of the images where the tumor amplitude is maximum. Table 3 reports the estimated and true location of the tumor, demonstrating that the SLSQ-DAS method gives the best solution. Table 4 shows the tumor localization values. After attenuation compensation, images have $\approx$ 1.5% more focusing of tumor response compared to that of the DAS image.

E. D4 DATASET
This dataset is acquired from the patient's right breast. To provide a reliable DAS image. we apply a lowpass filter with a cutoff frequency of 4.5 GHz [48]. Fig. 11(a) shows the data before and after skin removal at channel 70. The data show similar attenuation behavior to that of the D2 dataset in Fig. 6(a), so we choose similar regularization parameters
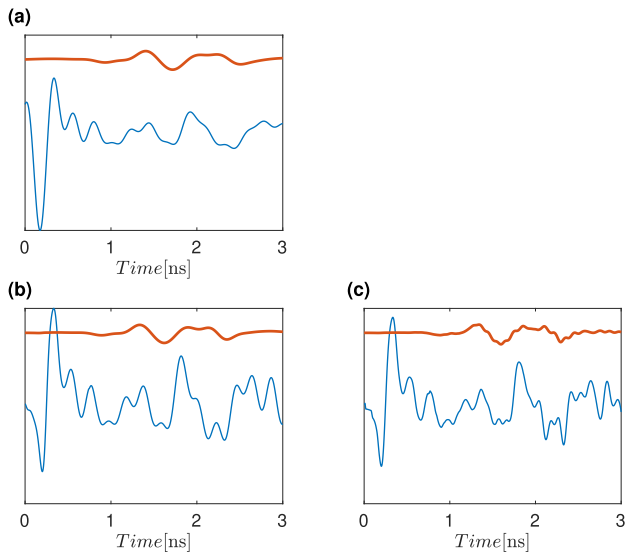
(a)

(b)   **(c)**

FIGURE 11. Performance of attenuation compensation algorithms on the patient (D4- right breast) data before and after skin removal. (a) measured dataset after low-pass filtering at channel 70 (blue color) and its corresponding data after skin removal (red color). (b), and (c) are the estimated data after attenuation compensation by using DLSQ and SLSQ methods on (a), respectively.
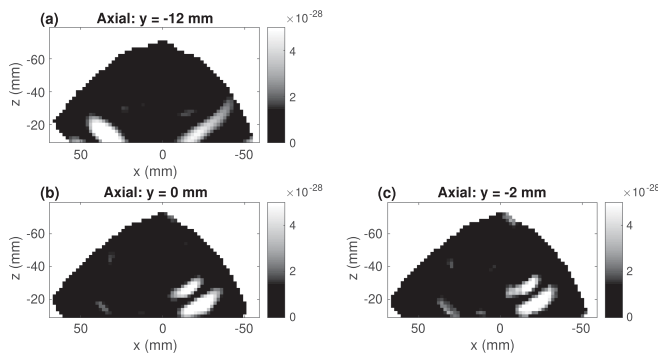

(a) Axial: y = -12 mm

(b) Axial: y = 0 mm   **(c)** Axial: y = -2 mm

FIGURE 12. Axial images of patient D4- right breast dataset. (a) DAS image. (b) DLSQ-DAS image. (c) SLSQ-DAS image.

(Table 2). The data after attenuation compensation are represented in Fig. 11(b)–(c).

Fig. 12 shows the axial images of the right breast with the DAS, DLSQ-DAS, and SLSQ-DAS methods. The subtle differences in the amplitude and phase of the data before and after attenuation compensation are responsible for the resolution and localization of the tumor in the images. Compared to the result of conventional DAS, the DLSQ-DAS, and SLSQ-DAS methods provide better-localized tumor responses. The coronal images of this dataset are shown in Fig. 13. Note that in DLSQ-DAS and SLSQ-DAS images, the maximum amplitude of the tumor is located in slightly different locations. The maximum locations of the tumor on the patient's right breast are summarized in Table 3. The locations show consistent results for DLSQ-DAS and SLSQ-DAS methods. Table 4 shows the tumor localization values. After attenuation compensation,
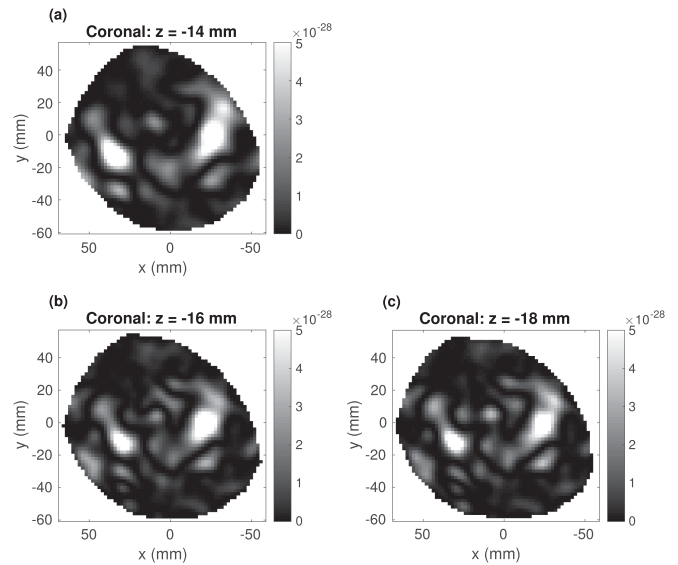

(a) Coronal: z = -14 mm

(b) Coronal: z = -16 mm   **(c)** Coronal: z = -18 mm

FIGURE 13. Coronal images of patient D4- right breast dataset. (a) DAS image. (b) DLSQ-DAS image. (c) SLSQ-DAS image.

images have 1.6% more focused tumor response compared to that of the DAS image.

IV. CONCLUSION

We introduced a non-stationary convolutional model, based on frequency-dependent attenuation, and developed an alternating minimization algorithm that simultaneously solves for the reflectivity series and the quality factor. We showed that to efficiently compensate for attenuation, adding regularization terms in the inversion process is necessary. After adding regularization terms, the algorithms were demonstrated to efficiently compensate for attenuation with simulated and experimental datasets. The attenuation-compensated data available from the algorithms were used to form images with DAS beamforming. The attenuation compensation provided better images in terms of the location of the tumor and tumor localization metrics.

Our future work aims to solve for varying quality factors instead of the constant Q model. In this work, we used constant frequency independent Q factor to define the attenuation in the breast tissue, where the Q_0 value in the algorithms was an approximate estimate of the average attenuation factor for the breast. The Q_0 value is different for fatty and fibroglandular tissues. Since the breast tissue is not a homogenous medium, ideally, we should consider the medium complexities in our Q modeling. For example, this may include considering frequency-dependent Q factor model, dielectric parameter changes for different tissues, and different Q factors for different sections of the breast. To provide a realistic Q model, we need to apply tomography to provide velocity information within the breast tissues and use an advanced Q model to change the velocities to Q factor values that can vary within the breast medium. Such a model can better define the medium, but it makes the algorithm very non-linear and

increases the number of unknowns. However, based on our extensive tests, we concluded that a constant Q model with a priori knowledge of Q_0 corresponding to the background medium provides promising results. Also, in practice, we can control the signal transmitted from the antenna. Since we could control the source, we assumed that we knew the signature of the transmitted pulse. However, if there is an error in the assumed signature, we need to modify the cost function and treat the transmission pulse signal as an unknown parameter. It is worth noting that the proposed processing algorithms can also be applied to any non-stationary data such as seismic, ground-penetrating radar, and ultrasound.

ACKNOWLEDGMENT

REFERENCES

[1] D. O'Loughlin, M. O'Halloran, B. M. Moloney, M. Glavin, E. Jones, and M. A. Elahi, "Microwave breast imaging: Clinical advances and remaining challenges," *IEEE Trans. Biomed. Eng.*, vol. 65, no. 11, pp. 2580–2590, Nov. 2018.

[2] E. Porter and D. O'Loughlin, "Pathway to demonstrating clinical efficacy of microwave breast imaging: Qualitative and quantitative performance assessment," *IEEE J. Electromagn., RF, Microw. Med. Biol.*, vol. 6, no. 4, pp. 439–448, Dec. 2022.

[3] N. Epstein, P. Meaney, and K. Paulsen, "3D parallel-detection microwave tomography for clinical breast imaging," *Rev. Sci. Instrum.*, vol. 85, no. 12, 2014, Art. no. 124704.

[4] C. Kaye, I. Jeffrey, and J. LoVetri, "Improvement of multi-frequency microwave breast imaging through frequency cycling and tissue-dependent mapping," *IEEE Trans. Antennas Propag.*, vol. 67, no. 11, pp. 7087–7096, Nov. 2019.

[5] B. M. Moloney et al., "Microwave imaging in breast cancer–results from the first-in-human clinical investigation of the wavelia system," *Academic Radiol.*, vol. 29, pp. S211–S222, 2022.

[6] M. Shere, I. Lyburn, R. Sidebottom, H. Massey, C. Gillett, and L. Jones, "MARIA M5: A multicentre clinical study to evaluate the ability of the micrima radio-wave radar breast imaging system (MARIA) to detect lesions in the symptomatic breast," *Eur. J. Radiol.*, vol. 116, pp. 61–67, 2019.

[7] B. Khalid et al., "3D Huygens principle based microwave imaging through MammoWave device: Validation through phantoms," *IEEE Access*, vol. 10, pp. 106770–106780, 2022.

[8] E. C. Fear, X. Li, S. C. Hagness, and M. A. Stuchly, "Confocal microwave imaging for breast cancer detection: Localization of tumors in three dimensions," *IEEE Trans. Biomed. Eng.*, vol. 49, no. 8, pp. 812–822, Aug. 2002.

[9] D. J. Kurrant, E. C. Fear, and D. T. Westwick, "Tumor response estimation in radar-based microwave breast cancer detection," *IEEE Trans. Biomed. Eng.*, vol. 55, no. 12, pp. 2801–2811, Dec. 2008.

[10] M. D. Hossain and A. S. Mohan, "Cancer detection in highly dense breasts using coherently focused time-reversal microwave imaging," *IEEE Trans. Comput. Imag.*, vol. 3, no. 4, pp. 928–939, Dec. 2017.

[11] H. Song et al., "A two-stage rotational surface clutter suppression method for microwave breast imaging with multistatic impulse-radar detector," *IEEE Trans. Instrum. Meas.*, vol. 69, no. 12, pp. 9586–9598, Dec. 2020.

[12] D. O'Loughlin et al., "Parameter search algorithms for microwave radar-based breast imaging: Focal quality metrics as fitness functions," *Sensors*, vol. 17, no. 12, 2017, Art. no. 2823.

[13] E. J. Bond, X. Li, S. C. Hagness, and B. D. V. Veen, "Microwave imaging via space-time beamforming for early detection of breast cancer," *IEEE Trans. Antennas Propag.*, vol. 51, no. 8, pp. 1690–1705, Aug. 2003.

[14] A. Shahzad, M. O'Halloran, E. Jones, and M. Glavin, "A preprocessing filter for multistatic microwave breast imaging for enhanced tumour detection," *Prog. Electromagn. Res.*, vol. 57, pp. 115–126, 2014.

[15] P. Kosmas and C. M. Rappaport, "FDTD-based time reversal for microwave breast cancer detection-localization in three dimensions," *IEEE Trans. Microw. Theory Techn.*, vol. 54, no. 4, pp. 1921–1927, Jun. 2006.

[16] N. Ghavami, P. P. Smith, G. Tiberi, D. Edwards, and I. Craddock, "Non-iterative beamforming based on Huygens principle for multistatic ultrawide band radar: Application to breast imaging," *IET Microw., Antennas Propag.*, vol. 9, no. 12, pp. 1233–1240, 2015.

[17] K. Y. Liu, E. C. Fear, and M. E. Potter, "Gabor nonstationary deconvolution for attenuation compensation in highly lossy dispersive media," *CREWES Res. Rep.*, vol. 27, pp. 1–22, 2015. [Online]. Available: https://www.crewes.org/Documents/ResearchReports/2015/CRR201546.pdf

[18] K. Y. Liu, E. C. Fear, and M. E. Potter, "Data preconditioning with gabor nonstationary deconvolution for radar imaging of highly dissipative and dispersive media," *Prog. Electromagn. Res.*, vol. 72, pp. 169–195, 2017.

[19] B. Maklad, C. Curtis, E. C. Fear, and G. G. Messier, "Neighborhood-based algorithm to facilitate the reduction of skin reflections in radar-based microwave imaging," *Prog. Electromagn. Res.*, vol. 39, pp. 115–139, 2012.

[20] G. F. Margrave, M. P. Lamoureux, and D. C. Henley, "Gabor deconvolution: Estimating reflectivity by nonstationary deconvolution of seismic data," *Geophysics*, vol. 76, no. 3, pp. W15–W30, 2011.

[21] J. C. Nash and M. Walker-Smith, *Nonlinear Parameter Estimation: An Integrated System in BASIC*. New York, NY, USA: Marcel Dekker, Inc., 1987.

[22] R. Dasgupta and R. A. Clark, "Estimation of Q from surface seismic reflection data," *Geophysics*, vol. 63, no. 6, pp. 2120–2128, 1998.

[23] C. Zhang and T. J. Ulrych, "Seismic absorption compensation: A least squares inverse scheme," *Geophysics*, vol. 72, no. 6, pp. R109–R114, 2007.

[24] C. Zhang and T. J. Ulrych, "Estimation of quality factors from CMP records," *Geophysics*, vol. 67, no. 5, pp. 1542–1547, 2002.

[25] P. D. O'grady, B. A. Pearlmutter, and S. T. Rickard, "Survey of sparse and non-sparse methods in source separation," *Int. J. Imag. Syst. Technol.*, vol. 15, no. 1, pp. 18–33, 2005.

[26] W. Li and J. C. Preisig, "Estimation of rapidly time-varying sparse channels," *IEEE J. Ocean. Eng.*, vol. 32, no. 4, pp. 927–939, Oct. 2007.

[27] J. Mairal, M. Elad, and G. Sapiro, "Sparse representation for color image restoration," *IEEE Trans. Image Process.*, vol. 17, no. 1, pp. 53–69, Jan. 2008.

[28] J. Wright, A. Y. Yang, A. Ganesh, S. S. Sastry, and Y. Ma, "Robust face recognition via sparse representation," *IEEE Trans. Pattern Anal. Mach. Intell.*, vol. 31, no. 2, pp. 210–227, Feb. 2009.

[29] M. Aharon and M. Elad, "Sparse and redundant modeling of image content using an image-signature-dictionary," *SIAM J. Imag. Sci.*, vol. 1, no. 3, pp. 228–247, 2008.

[30] K. E. Leung et al., "Sparse registration for three-dimensional stress echocardiography," *IEEE Trans. Med. Imag.*, vol. 27, no. 11, pp. 1568–1579, Nov. 2008.

[31] E. J. Candes, M. B. Wakin, and S. P. Boyd, "Enhancing sparsity by reweighted ℓ_1 minimization," *J. Fourier Anal. Appl.*, vol. 14, no. 5-6, pp. 877–905, 2008.

[32] N. Kazemi and M. D. Sacchi, "Sparse multichannel blind deconvolution," *Geophysics*, vol. 79, no. 5, pp. V143–V152, 2014, doi: 10.1190/geo2013-0465.1.

[33] M. Azghani, P. Kosmas, and F. Marvasti, "Microwave medical imaging based on sparsity and an iterative method with adaptive thresholding," *IEEE Trans. Med. Imag.*, vol. 34, no. 2, pp. 357–365, Feb. 2015.

[34] N. Kazemi, E. Bongajum, and M. D. Sacchi, "Surface-consistent sparse multichannel blind deconvolution of seismic signals," *IEEE Trans. Geosci. Remote Sens.*, vol. 54, no. 6, pp. 3200–3207, Jun. 2016.

[35] A. Beck and M. Teboulle, "A fast iterative shrinkage-thresholding algorithm for linear inverse problems," *SIAM J. Imag. Sci.*, vol. 2, no. 1, pp. 183–202, 2009.

[36] R. Mises and H. Pollaczek-Geiringer, "Praktische Verfahren der Gleichungsauflösung," *ZAMM- J. Appl. Math. Mech./Zeitschrift für Angewandte Mathematik und Mechanik*, vol. 9, no. 1, pp. 58–77, 1929, doi: 10.1002/zamm.19290090105. [Online]. Available: https://onlinelibrary.wiley.com/doi/abs/10.1002/zamm.19290090105

[37] B. Noble, *Applied Linear Algebra*. Hoboken, NJ, USA: Prentice-Hall, 1969.

[38] G. Wahba, "The approximate solution of linear operator equations when the data are noisy," *Adv. Appl. Probability*, vol. 8, no. 2, pp. 222–223, 1976.

[39] D. J. Cummins, T. G. Filloon, and D. Nychka, "Confidence intervals for nonparametric curve estimates: Toward more uniform pointwise coverage," *J. Amer. Stat. Assoc.*, vol. 96, no. 453, pp. 233–246, 2001.

[40] F.-X. Dupé, J. M. Fadili, and J.-L. Starck, "A proximal iteration for deconvolving Poisson noisy images using sparse representations," *IEEE Trans. Image Process.*, vol. 18, no. 2, pp. 310–321, Feb. 2009.

[41] A. Gholami and M. D. Sacchi, "A fast and automatic sparse deconvolution in the presence of outliers," *IEEE Trans. Geosci. Remote Sens.*, vol. 50, no. 10, pp. 4105–4116, Oct. 2012.

[42] N. Kazemi, "Automatic blind deconvolution with Toeplitz-structured sparse total least squares," *Geophysics*, vol. 83, no. 6, pp. V345–V357, 2018.

[43] H. Szu and R. Hartley, "Fast simulated annealing," *Phys. Lett. A*, vol. 122, no. 3-4, pp. 157–162, 1987.

[44] J. Garrett and E. Fear, "A new breast phantom with a durable skin layer for microwave breast imaging," *IEEE Trans. Antennas Propag.*, vol. 63, no. 4, pp. 1693–1700, Apr. 2015.

[45] B. R. Lavoie, J. Bourqui, E. C. Fear, and M. Okoniewski, "Metrics for assessing the similarity of microwave breast imaging scans of healthy volunteers," *IEEE Trans. Med. Imag.*, vol. 37, no. 8, pp. 1788–1798, Aug. 2018.

[46] J. Bourqui, M. Kuhlmann, D. J. Kurrant, B. R. Lavoie, and E. C. Fear, "Adaptive monostatic system for measuring microwave reflections from the breast," *Sensors*, vol. 18, no. 5, 2018, Art. no. 1340.

[47] D. Kurrant, J. Bourqui, C. Curtis, and E. Fear, "Evaluation of 3-D acquisition surfaces for radar-based microwave breast imaging," *IEEE Trans. Antennas Propag.*, vol. 63, no. 11, pp. 4910–4920, Nov. 2015.

[48] C. Curtis, B. R. Lavoie, and E. Fear, "An analysis of the assumptions inherent to near-field beamforming for biomedical applications," *IEEE Trans. Comput. Imag.*, vol. 3, no. 4, pp. 953–965, Dec. 2017.

NASSER KAZEMI received the Ph.D. degree in geophysics from the University of Alberta, Edmonton, AB, Canada, in 2017. He was a Postdoctoral Fellow with the Petroleum Engineering Department, University of Calgary, Calgary, AB, Canada, till 2022. Then he joined the Université du Québec à Montréal, Montreal, QC, Canada, as an Assistant Professor of applied geophysics. His research interests include developing algorithms for signal processing and imaging of geophysical data.

ELISE FEAR (Senior Member, IEEE) received the Ph.D. degree in electrical engineering from the University of Victoria, Victoria, BC, Canada, in 2001. Then she joined the University of Calgary, Calgary, AB, Canada, where she is currently a Professor with the Department of Electrical and Software Engineering. Her research interests in imaging and sensing include the development of novel microwave imaging and sensing systems for medical applications, as well as pre-clinical evaluation of these technologies.